Available online at www.sciencedirect.com

ScienceDirect

Advances in Space Research xxx (2020) xxx–xxx

ADVANCES IN SPACE RESEARCH (a COSPAR publication)

www.elsevier.com/locate/asr

A Partially Orthogonal EnKF approach to atmospheric density estimation using orbital debris

Shaylah Mutschler *, Penina Axelrad, Tomoko Matsuo

University of Colorado Boulder, Aerospace Engineering Sciences, 3775 Discovery Dr., Boulder, CO 80303, USA

Received 25 August 2019; received in revised form 7 November 2019; accepted 22 January 2020

Abstract

A key requirement for accurate trajectory prediction and space situational awareness is knowledge of how non-conservative forces affect space object motion. These forces vary temporally and spatially, and are driven by the underlying behavior of space weather particularly in Low Earth Orbit (LEO). Existing trajectory prediction algorithms adjust space weather models based on calibration satellite observations. However, lack of sufficient data and mismodeling of non-conservative forces cause inaccuracies in space object motion prediction, especially for uncontrolled debris objects. The uncontrolled nature of debris objects makes them particularly sensitive to the variations in space weather. Our research takes advantage of this behavior by utilizing observations of debris objects to infer the space environment parameters influencing their motion.

The hypothesis of this research is that it is possible to utilize debris objects as passive, indirect sensors of the space environment. We focus on estimating atmospheric density and its spatial variability to allow for more precise prediction of LEO object motion. The estimated density is parameterized as a grid of values, distributed by latitude and local sidereal time over a spherical shell encompassing Earth at a fixed altitude of 400 km. The position and velocity of each debris object are also estimated. A Partially Orthogonal Ensemble Kalman Filter (POEnKF) is used for assimilation of space object measurements to estimate density.

For performance comparison, the scenario characteristics (number of objects, measurement cadence, etc.) are based on a sensor tasking campaign executed for the High Accuracy Satellite Drag Model project. The POEnKF analysis details spatial comparisons between the true and estimated density fields, and quantifies the improved accuracy in debris object motion predictions due to more accurate drag force models from density estimates. It is shown that there is an advantage to utilizing multiple debris objects instead of just one object. Although the work presented here explores the POEnKF performance when using information from only 16 debris objects, the research vision is to utilize information from all routinely observed debris objects. Overall, the filter demonstrates the ability to estimate density to within a threshold of accuracy dependent on measurement/sensor error. In the case of a geomagnetic storm, the filter is able to track the storm and provide more accurate density estimates than would be achieved using a simple exponential atmospheric density model or MSIS Atmospheric Model (when calm conditions are assumed).

Keywords: Orbital debris; Atmospheric density; EnKF; Space weather; Space situational awareness; Particle Filter

1. Introduction

Our research proposes to utilize debris objects to sense their local space environment. A multi-object filter is used to extract the underlying non-conservative forces without a detailed physical description of the individual objects. The end goal is a data assimilation framework capable of handling high dimensional systems with nonlinear dynamics and leveraging all available observations. We focus on the low Earth orbital regime where mismodeling of atmospheric drag is the largest contributor to orbit prediction

* Corresponding author.
E-mail address: shaylah.mutschler@colorado.edu (S. Mutschler).

https://doi.org/10.1016/j.asr.2020.01.021
0273-1177/

error. However, it is expected that the methods developed could be extended to additional orbital regimes for refinement of magnetic field and solar radiation models.

This work explores a problem in which we use multiple debris objects to estimate atmospheric density parameters, as well as the position and velocity of each debris object. The purpose of this article is to explore the combined orbit and density estimation problem to determine the system requirements, such as the number of ground sensors, measurement cadence, and ballistic coefficient knowledge. We also analyze the performance of the tool during a simulated geomagnetic storm in which the atmospheric density magnitude rapidly increases.

1.1. Atmospheric density

An object in Low Earth Orbit (LEO) experiences atmospheric drag caused by particles in the atmosphere colliding with the surface of the object. Drag acts primarily in the opposite direction of the velocity vector to decrease the speed of an object. The magnitude of the force due to drag is directly dependent on neutral density (number of particles in the atmosphere). This is illustrated in the equation of acceleration due to drag,

$$a_{drag} = -\frac{1}{2}\rho\frac{C_D A}{m}v_{rel}^2\frac{\vec{v}_{rel}}{|\vec{v}_{rel}|} \tag{1}$$

where

$$\vec{v}_{rel} = \frac{d\vec{r}}{dt} - \vec{\omega}_{\oplus}\times\vec{r} \tag{2}$$

is the velocity vector relative to the rotating atmosphere, C_D is the coefficient of drag, A is the exposed cross-sectional area, m is the object's mass, $\vec{\omega}_{\oplus}$ is the mean motion of the Earth's rotation, and $\vec{r}$ is the Earth Centered Inertial object position vector (Vallado, 2013). The drag coefficient, mass, and area of the object are typically combined to form the ballistic coefficient ($\beta = \frac{C_D A}{m}$).

Atmospheric density is highly dynamic and depends on a number of factors, including solar cycle, diurnal cycle, geomagnetic activity, altitude, and latitude. Atmospheric models are used in orbital object prediction. A potential discrepancy between model and reality may lead to relatively large errors in orbit prediction. If a model assumes calm conditions, i.e. little to no geomagnetic activity, it produces an atmospheric density of about 0.0015 g/km^3 at 400 km altitude (using Ap and F10.7 indices of 17 and 127, respectively). On the other hand, when a geomagnetic storm hits, the density can rise more than an order of magnitude to 0.037 g/km^3 within minutes. This density value corresponds to input parameters, Ap and F10.7 indices, being set to 400 and 273, respectively in the MSIS (Mass Spectrometer and Incoherent Scatter) Atmospheric Model (Picone et al., 2002). Our research aims to estimate the atmospheric density in real time, specifically considering potential variability due to the diurnal cycle, latitude, and geomagnetic activity.

1.2. Previous work

Current methods that estimate or model atmospheric density can be categorized as either empirical or physics-based approaches. Empirical models are computationally fast, but only represent the climatological atmospheric conditions. Physics-based models incorporate current knowledge of atmospheric conditions to provide forecasts, but require substantially more computing power than empirical models.

An example of an empirical approach is the High Accuracy Satellite Drag Model (HASDM) project. This effort estimates a time-series of thirteen spherical harmonic global density correction coefficients by using observations of 75–80 carefully selected calibration satellites (payloads and debris) in a batch fit (Bowman and Storz, 2002, 2003; Storz et al., 2005). Intensive sensor tasking is made available for this effort, which allows for the collection of approximately 500 observations per day per calibration satellite. A batch fit solves for both temperature and density correction coefficients. HASDM decouples the ballistic coefficient and the density parameter by first solving for the long-term averaged ballistic coefficient of each satellite. This ballistic coefficient is computed by averaging almost 3200 previously estimated ballistic coefficients of each calibration satellite.

The Direct Density Correction Method (DDCM) project takes a slightly different approach by using Two-Line Element sets (TLE) of sixteen well-known objects (Yurasov et al., 2005, 2006). DDCM empirically estimates two time-series density correction coefficients for both the MSIS Atmospheric Model (Picone et al., 2002) and the Russian "Upper Atmosphere Model for Ballistic Calculations," known as GOST (Volkov, 2004), density models. The DDCM method includes secondary data processing in which smoothed orbits of each object and smoothed ballistic coefficients are estimated. This smoothing approach enables only long-period variations in density to be observable, which is a drawback of the DDCM effort.

The HASDM and DDCM empirical models do not allow for the spatial and temporal resolution necessary to capture the dynamical behavior of density. As described above, these methods estimate coefficients of density that are applied to a pre-defined model, not density directly. Furthermore, by combining information from objects in different regimes, or at different altitudes, a single batch fit limits the spatial resolution of density corrections that can be achieved.

More recently, density modeling and forecasting methods have been developed that take advantage of physics-based models. Matsuo (2014) showed that ionospheric electron density data can be used with a physics-based model to estimate and predict thermospheric mass density. Electron density data are assimilated with an Ensemble

Please cite this article as: S. Mutschler, P. Axelrad and T. Matsuo, A Partially Orthogonal EnKF approach to atmospheric density estimation using orbital debris, Advances in Space Research, https://doi.org/10.1016/j.asr.2020.01.021

Kalman Filter (EnKF) to estimate input, or driver parameters of the physics-based Thermosphere-Ionosphere-Electrodynamics General circulation model (TIE-GCM). These drivers include thermospheric temperature and composition. Her work demonstrates that assimilation of COSMIC/FORMOSAT-3 electron density data can extend thermospheric mass density predictions produced by TIE-GCM by more than three days.

Mehta and Linares (2017) developed an approach that aims to combine the strength of a physics based model in its predictive capability, with the speed of an empirical model. In their approach, a reduced order model captures the upper atmospheric dynamics by using proper orthogonal decomposition to project a high dimensional system onto a set of low-order basis functions. This approach is demonstrated using an empirical model, MSIS, as the underlying upper atmosphere model with the intention that a physics-based model will replace MSIS in the future.

A physics-based approach that estimates atmospheric drivers, such as F10.7 and Kp indices, as inputs to TIE-GCM is described by Sutton (2018). This effort estimates drivers through an iterative process that involves data assimilation of neutral density data from Challenging Mini-Satellite Payload (CHAMP). Each iteration initializes several instances of an Ionosphere-Thermosphere (I-T) model with an ensemble of drivers. An updated driver estimate is formed via the measurement update that assesses the agreement between each I-T model instance and the neutral density data. Once convergence between the I-T model and density data is reached, the driver estimates can be used with TIE-GCM to provide atmospheric forecasts.

Our proposed density estimation method is introduced in Section 2. A comparison is presented between two nonlinear estimation filters, the Particle Filter (PF) and Ensemble Kalman Filter (EnKF), and the decision to use the Partially Orthogonal EnKF (POEnKF) as the chosen data assimilation tool is discussed. A simple example of a density estimation problem is introduced in Section 3 to compare the performance of the PF and POEnKF. Section 4 describes the full density estimation scenario and the performance of the PoEnKF when applied to this system is analyzed in Section 5.

2. Method

Unlike current methods, our research estimates density from ground-based observations of object trajectories. This work also aims to take advantage of all debris objects, instead of a small, handpicked portion of the resident space object (RSO) population. This approach allows for a higher resolution density estimate. The resolution of the density estimate is dependent on its spatial parameterization and the available debris object distribution; details of the current parameterization scheme are given in Section 4.1.

When limited to metric data, the ballistic coefficient and density terms cannot be decoupled if debris object physical characteristics are unknown, precluding the explicit estimation of density. (Interestingly, it has been shown that the ballistic coefficient and density terms can be decoupled if photometric data are utilized (Linares et al., 2014).) The work presented here aims to utilize all debris objects, objects that are typically not characterized. To resolve this, a density calibration tool, such as HASDM, is leveraged to provide initial density estimates. These estimates are combined with debris object tracking information to solve for initial object ballistic coefficients. Once this "bootstrapping" process is complete, our density estimation method begins using the recently solved for ballistic coefficients.

2.1. Particle Filter v. Ensemble Kalman Filter

Nonlinear systems pose challenges in estimation that require special filtering methods and numerical techniques to handle non-Gaussian distributions that result from nonlinear dynamics and/or measurements. Two filters commonly used for nonlinear systems are the PF and the EnKF. The Particle Filter was introduced in 1993 and is known as a truly nonlinear filter because no Gaussian or linear assumptions are made in its formulation (Gordon et al., 1993). The EnKF was introduced to estimate high-dimensional systems in a computationally tractable manner (Evensen, 1994). It does so by combining Kalman filter theory and Monte Carlo estimation methods (Houtekamer and Zhang, 2016).

An obvious commonality between the two filters is that they take advantage of a particle representation of the state PDF. The number of particles (N) required is an obvious difference between the filters. The PF requires at least 10^n (n is the number of state elements) weighted particles to capture the full non-Gaussian PDF, while the EnKF uses an ensemble of state realizations, or "particles," of size greater than $2n+1$ (number of particles used in the Unscented Kalman Filter) and less than 10^n. In the EnKF, N is determined via a Monte Carlo study; there is no exact definition for N in the EnKF as there is in the PF and Unscented Kalman Filter. The number of particles in each filter is a direct indication of the level of nonlinearity the filter maintains. Although the PF maintains the full nonlinearity behavior of a system, it has a major obvious pitfall associated with the requirement of 10^n particles which becomes intractable for states with more than 5 elements (dimensionality curse). On the other hand, a well known strength of the EnKF is its ability to handle high-dimensional systems. Section 3 introduces an example of a nonlinear high-dimension system, a density estimation problem, in which a comparison between the performance of a PF and EnKF will be discussed.

Please cite this article as: S. Mutschler, P. Axelrad and T. Matsuo, A Partially Orthogonal EnKF approach to atmospheric density estimation using orbital debris, Advances in Space Research, https://doi.org/10.1016/j.asr.2020.01.021

2.2. The EnKF approach

The Ensemble Kalman Filter (EnKF) is typically used in high-dimensional nonlinear geophysical applications, such as forecasting of atmosphere and ocean systems, where there is an abundance of observations (Houtekamer and Zhang, 2016). Our research applies the EnKF to a combination of a large-scale problem and a smaller scale problem. The latter is a typical orbit determination (OD) problem in which the position and velocity of the tracked objects are estimated. The large-scale portion is a high-dimensional geospatial estimation problem of the density field. Each of the N ensemble members are represented by $\chi_k^{(i)}$, where $1 < i < N$ and k denotes time-step. For this work, we use a variant of the Ensemble Kalman Filter, the POEnKF (Heemink et al., 2000); as described in the following.

2.3. Partially Orthogonal EnKF

Due to a lack of observability, the EnKF might suffer from a nonpositive definite covariance. A common solution to this issue is localization, which effectively localizes the measurement update to state elements close to the measurement. A smaller portion of the state correction is applied to elements farther from the measurement (Houtekamer and Zhang, 2016). One example of a localization function is applying a ratio of the correction; the ratio is defined by an exponential function ($\mathcal{C}$), dependent on distance from the measurement:

$$\chi_k^{(i)+} = \chi_k^{(i)-} + \mathcal{C} * K\left(y_k^o - \mathcal{Y}^{(i)}\right) \tag{3}$$

where K is the Kalman gain, y^o is a uniquely perturbed observation, and $\mathcal{Y}$ is the predicted measurement (Gaspari and Cohn, 1999).

We use the MSIS Atmospheric Model (Picone et al., 2002) to generate the density field through which we simulate debris object trajectories. Due to the globally coherent dynamical behavior of density represented by MSIS, localization is not an option. The POEnKF provides an alternate approach to localization that maintains the full-rank covariance. It approximates the initial full covariance matrix with a reduced rank matrix by selecting its q leading eigenvectors (Heemink et al., 2000). The POEnKF is an effective solution to a weakly ranked covariance in a system like ours where the underlying model does not allow for localization. It does so by combining the EnKF and Reduced Rank EnKF (RREnKF) algorithms.

Following Heemink et al. (2000), the first step of the POEnKF is to select q, the number of leading eigenvectors to be used in the covariance approximation. This step helps form the L matrix, which is part of the RREnKF portion of the POEnKF. First, the initial covariance matrix is computed:

$$P_0^- = \frac{1}{N-1} E_0 E_0^T \tag{4}$$

where N is the number of ensemble members,

$$E_0^- = \left[\chi_0^{(1)-} - \overline{X}_0, \chi_0^{(2)-} - \overline{X}_0, \ldots, \chi_0^{(N)-} - \overline{X}_0\right] \tag{5}$$

and

$$\overline{X}_0 = \frac{1}{N}\sum_{i=1}^{N} \chi_0^{(i)} \tag{6}$$

The eigenvectors ($l_0^{(j)}$) and eigenvalues ($\lambda^{(j)}$) of the initial covariance matrix, P_0^-, are calculated and analyzed to select an appropriate number of leading eigenvectors for the reduced rank approximation.

$$L_0 = \left[l_0^{(1)}, l_0^{(2)}, \ldots, l_0^{(q)}\right] \tag{7}$$

where

$$P_0^- \overrightarrow{v}^{(j)} = \lambda^{(j)} \overrightarrow{v}^{(j)} \tag{8}$$

and

$$l_0^{(j)} = \sqrt{\lambda^{(j)}}\ \overrightarrow{v}^{(j)} \tag{9}$$

L is a matrix of the q leading eigenvectors ($l_0^{(j)}$), normalized by the square root of the eigenvalues (Eqs. (7)–(9)) (Heemink et al., 2000). The superscript j is used to denote indices of q leading eigenvectors; whereas, the superscript i is used to denote the indices of N ensemble members. The q selection for our particular system is described in Section 4.5.

The POEnKF applies a linear update to a prior, non-Gaussian distribution, making it a partially nonlinear filter (Evensen, 2009). The particles take on a non-Gaussian distribution in the case of a nonlinear problem and are not forced to form a Gaussian distribution at any point in the filter. However, the measurement update is based only on the covariance, making the update linear. As a result, the solution of the EnKF is described by Evensen as "something between a linear Gaussian update and a full Bayesian computation" (Evensen, 2009).

A Monte Carlo method is employed in the form of an ensemble representation of the estimated state probability distribution. The ensemble contains N members where each member is a sample realization of the state that is drawn from a normal distribution. Combined, the ensemble members represent the *a priori* distribution of the state and define the initial mean and variance of each state element. An ensemble representation of the initial state is generated using the *a priori* statistical information of the state X as shown in Eq. (10).

The POEnKF ensemble initialization and forecast step are similar to the EnKF with the addition of a matrix L, the reduced rank, square root of the forecast covariance given in Eq. (7) (Heemink et al., 2000) as follows

$$\chi_0^{(i)} = \overrightarrow{X}_0 + \eta^{(i)} \tag{10}$$

where $\eta^{(i)}$ is a realization of the process noise.

$$\chi_k^{(i)-} = \mathcal{M}\left(\chi_{k-1}^{(i)+}\right) + w^{(i)} \tag{11}$$

Please cite this article as: S. Mutschler, P. Axelrad and T. Matsuo, A Partially Orthogonal EnKF approach to atmospheric density estimation using orbital debris, Advances in Space Research, https://doi.org/10.1016/j.asr.2020.01.021

$$w^{(i)} \sim \mathcal{N}(0, Q) \tag{12}$$

The POEnKF time update is the nonlinear propagation of the state ensemble (Eq. (11)) (Houtekamer and Mitchell, 2005), where $\mathcal{M}$ is the nonlinear forecast operator. Superscript (i) denotes the ith ensemble member. The L matrix is updated in the forecast step:

$$\overline{X}_{k-1} = \frac{1}{N}\sum_{i=1}^{N} \chi_{k-1}^{(i)+} \tag{13}$$

$$l_k^{(j)-} = \frac{1}{\epsilon}\left[\mathcal{M}\left(\overline{X}_{k-1} + \epsilon l_{k-1}^{(j)+}\right) - \mathcal{M}\left(\overline{X}_{k-1}\right)\right] \tag{14}$$

where ϵ is a perturbation that is set to equal 0.95. The L matrix represents the effect that a relatively small perturbation has on an ensemble member during the forecast step and is computed by Eq. (14).

The prior covariance is computed as

$$P_k^- = \gamma L_k^- L_k^{-T} + \frac{1-\gamma}{N-1} E_k''^- E_k''^{-T} \tag{15}$$

where $0 \leqslant \gamma \leqslant 1$ is a weighting coefficient and a smaller γ is better for nonlinear systems (γ= 0.4 is used). Information from the POEnKF q leading eigenvectors is provided by the first term, $L_k^- L_k^{-T}$ (RREnKF portion of the POEnKF), and information from the full ensemble is incorporated via the second term, $E_k''^- E_k''^{-T}$. $E_k''^-$ is the projection of the ensemble members onto the q leading eigenvectors and is computed as follows:

$$E_k^{-T} E_k^- = X\Omega X^T \tag{16}$$

$$E_k''^- = \left[E_k^- X\right]_{:,1:q} \tag{17}$$

It should be noted that in the implementation of Eq. (15) shown in Heemink et al. (2000), there is an additional contribution of the covariance projected in directions orthogonal to the space spanned by the ensemble $l_k^{(j)-}$. This term is intended to rectify the problem of rank-deficiency of the ensemble-based covariance matrix by modifying the covariance matrix in a way to increase its rank (Evensen, 2009). Our filtering experiments have performed well without an inclusion of this additional covariance contribution. If issues of rank-deficiency in the context of this specific application arise, an effective way to remedy them will be investigated in the future.

The state measurement update is analogous to the EnKF with the addition of the L matrix and modified covariance update:

$$y_k^o = \tilde{y}_k + \epsilon \tag{18}$$

$$\epsilon \sim \mathcal{N}(0, R) \tag{19}$$

$$\mathcal{Y}_k^{(i)} = \mathcal{G}\left(\chi_k^{(i)-}\right) \tag{20}$$

$$\chi_k^{(i)+} = \chi_k^{(i)-} + K\left(y_k^o - \mathcal{Y}^{(i))}\right) \tag{21}$$

$$\overrightarrow{X}_k = \frac{1}{N}\sum_{i=1}^{N} \chi_k^{(i)+} \tag{22}$$

where $\mathcal{G}$ is the measurement equation as a function of the state, $\mathcal{Y}$ is the predicted measurement, and R is the measurement covariance matrix. The measurement update for each POEnKF member (Eq. (18)) incorporates a uniquely perturbed observation, y^o for each ensemble member. This is a signature feature of the stochastic EnKF not used in other nonlinear filters. The Kalman gain is calculated in a conventional manner as follows

$$K = P_k^- H^T \left[H P_k^- H^T + R\right]^{-1} \tag{23}$$

where H is the Jacobian matrix, i.e. the partial derivative of the measurement models ($\overrightarrow{Y}$) with respect to the state

$$H = \left[\frac{\partial \overrightarrow{Y}}{\partial \overrightarrow{X}}\right] \tag{24}$$

and the covariance update is computed as follows:

$$\tilde{L}_k^+ = \left[(I - KH)L_k^-,\ KR^{\frac{1}{2}}\right] \tag{25}$$

$$\tilde{L}_k^{+T} \tilde{L}_k^+ = X\Omega X^T \tag{26}$$

$$L_k^+ = \left[\tilde{L}_k^+ X\right]_{:,1:q} \tag{27}$$

$$E_k^{+T} E_k^+ = X\Omega X^T \tag{28}$$

$$E_k''^+ = \left[E_k^+ X\right]_{:,1:q} \tag{29}$$

$$P_k^+ = \gamma L_k^+ L_k^{+T} + \frac{1-\gamma}{N-1} E_k''^+ E_k''^{+T} \tag{30}$$

3. Simplified example of density estimation problem

A 2D simplified version of an OD and atmospheric density estimation problem is created to illustrate the POEnKF and the PF for high dimensional systems. The full version of the density estimation problem is introduced in Section 4.

3.1. System details and initialization

A scenario is created in which a single orbital debris object is utilized to estimate atmospheric density along its trajectory. The debris object trajectory is propagated using two-body Keplerian dynamics with the addition of acceleration due to atmospheric drag,

$$\ddot{\overrightarrow{X}} = \frac{\mu}{\overrightarrow{r}^3}\overrightarrow{r} - \frac{1}{2}\rho\frac{C_D A}{m} v_{rel}^2 \frac{\overrightarrow{v}_{rel}}{\left|\overrightarrow{v}_{rel}\right|} \tag{31}$$

where $\overrightarrow{v}_{rel}$ is defined in Eq. (2). The debris object is in a near circular, equatorial orbit at 400 km altitude; range and range-rate measurements of the object are collected from an inertially fixed sensor located at [0, R_{Earth}, 0].

For this simplified system, the atmospheric density is modeled as a partial sinusoid that varies as a function of Local Sidereal Time (LST) with a peak in density at local noon (LST 12),

$$\rho = A * sin(B * LST) + C \tag{32}$$

Please cite this article as: S. Mutschler, P. Axelrad and T. Matsuo, A Partially Orthogonal EnKF approach to atmospheric density estimation using orbital debris, Advances in Space Research, https://doi.org/10.1016/j.asr.2020.01.021

Fig. 1 shows the nominal density state as a function of LST. The debris object is simulated for a duration of 400 min. The true density through which the object passes is shown in Fig. 2.

The goal of this problem is to estimate the density field that the debris object is orbiting through, along with the X and Y position and X and Y velocity of a debris object (OD state). The density field portion of the state is located at the equator at the altitude corresponding to the debris object orbit, and is parameterized by LST with a 5 degree resolution (72 elements).

A perturbation is applied to the true initial OD state so that the *a priori* state in the filter is not equal to the true initial state,

$$\vec{X}'_{OD\ 0} = \vec{X}_{OD\ 0} + p_{OD} \tag{33}$$

where the perturbation (p_{OD}) has a nonzero mean ($\mu_{pert\ OD}$):

$$p_{OD} \sim \mathcal{N}(\mu_{pert\ OD}, P_{pert\ OD}) \tag{34}$$

$$\mu_{pert\ OD} = [10m, 10m, 0.1m/s, 0.1m/s]^T \tag{35}$$

$$P_{pert\ OD} = diag\left(\left[(1m)^2, (1m)^2, (.01m/s)^2, (.01m/s)^2\right]\right) \tag{36}$$

The OD state ensemble is generated using the perturbed initial state ($\vec{X}'_{OD\ 0}$) and its *a priori* statistical information (P_0):

$$\chi^{(i)}_{OD\ 0} = \vec{X}'_{OD\ 0} + \eta^{(i)} \tag{37}$$

where

$$\eta^{(i)} \sim \mathcal{N}(0, P_0) \tag{38}$$

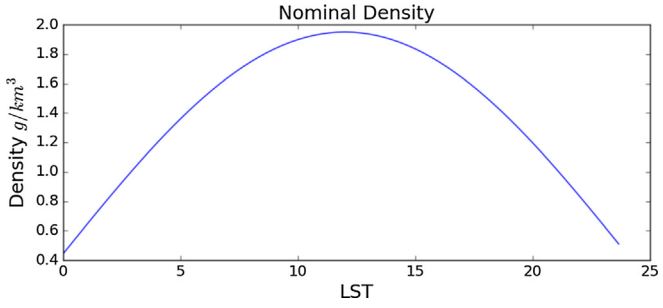

Fig. 1. True Density vs. LST Generated from Eq. (32), where A = 1.5 g/km^3, B = $\frac{2\pi}{48}$ hours, and C = 0.4 g/km^3.

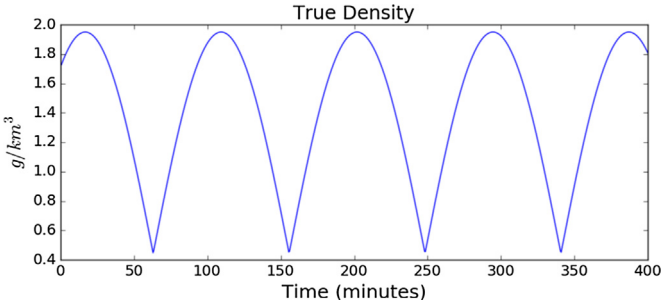

Fig. 2. Underlying true density vs. time.

and

$$P_0 = diag\left(\left[(10m)^2, (10m)^2, (.1m/s)^2, (.1m/s)^2\right]\right) \tag{39}$$

Similar to the OD state initial estimate, the initial filter estimate is perturbed from the true initial density:

$$\vec{X}'_{\rho\ 0} = \vec{X}_{\rho\ 0} + p_\rho \tag{40}$$

where,

$$p_\rho \sim \mathcal{N}(\mu_{pert\ \rho}, P_{pert\ \rho}) \tag{41}$$

$$\mu_{pert\ \rho} = [0.1, 0.1, \ldots, 0.1] g/km^3 \tag{42}$$

$$P_{pert\ \rho} = diag\left(\left[(5e^{-2})^2, (5e^{-2})^2, \ldots, (5e^{-2})^2\right]\right)(g/km^3)^2 \tag{43}$$

Next, the initial density state ensemble is generated by varying the vertical shift of the perturbed initial state ($\vec{X}'_{\rho\ 0}$) sinusoid. This approach reflects the behavior of a density ensemble generated via the MSIS model (Picone et al., 2002), where input parameters simply control the magnitude of the density state, but do not affect its spatial variability. The resulting density ensemble is shown in Fig. 3; each line represents the density state of one ensemble member.

With 76 state elements required, an ensemble size (N) of 150 members is used in the POEnKF. The theoretically required number of particles for the PF (10^{76} particles) causes the filter to be computationally intractable for this high dimensional system, so 10^4 particles are used in the PF implementation. This number of particles is chosen because the filter can run in about double the amount of time as the POEnKF.

3.2. Results and analysis

Both the PF and POEnKF are applied to this simplified density estimation system and their performance is compared. Fig. 4 shows the PF density estimate percent error. The estimate is more accurate in the beginning of the simulation but then quickly veers off track. This is due to the insufficient number of particles used (10^4 instead of 10^{76} particles). The evolution of the PF particles is shown in Fig. 6. It is apparent that the particle distribution quickly collapses and, therefore underrepresents the full state space probability (Fig. 5). This causes the covariance to collapse and the filter to discard information from the measurements.

Unlike the PF, the POEnKF is able to recover the true density to within 10% error after 100 min, as shown in Fig. 7. The POEnKF's particle, or ensemble member distribution accurately captures the probable state space and the estimate error magnitude.

The evolution of ensemble members is shown in Fig. 8 with the same axis bounds as the PF (Fig. 6). After estimate convergence at 100 min (shown in Fig. 7), the distribution

Please cite this article as: S. Mutschler, P. Axelrad and T. Matsuo, A Partially Orthogonal EnKF approach to atmospheric density estimation using orbital debris, Advances in Space Research, https://doi.org/10.1016/j.asr.2020.01.021

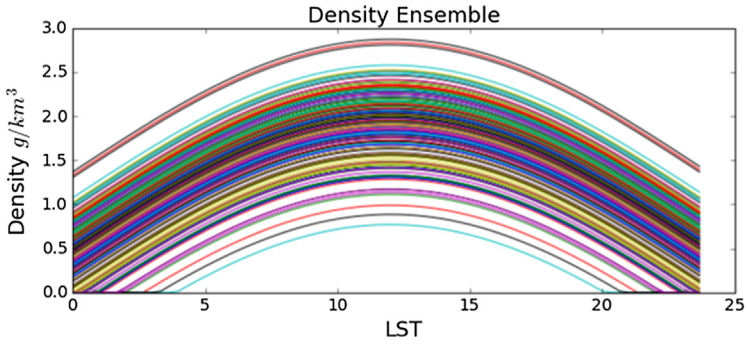

Fig. 3. Density ensemble generated from perturbed initial state.

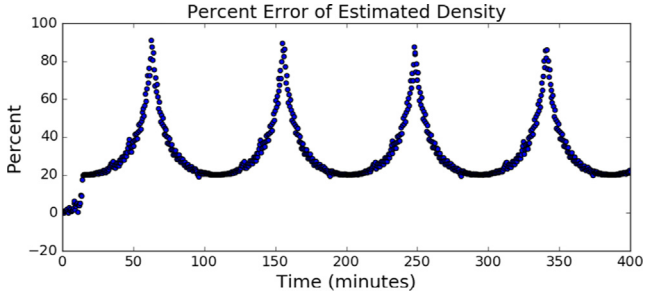

Fig. 4. PF density estimate percent error.

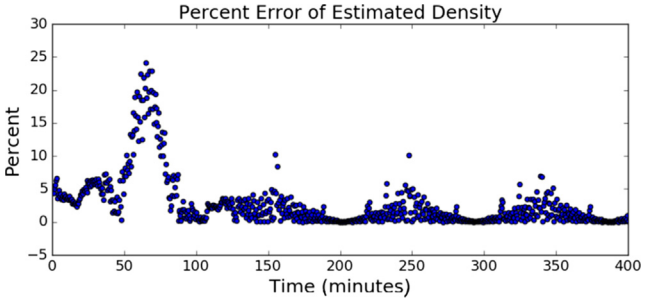

Fig. 7. POEnKF density estimate percent error.

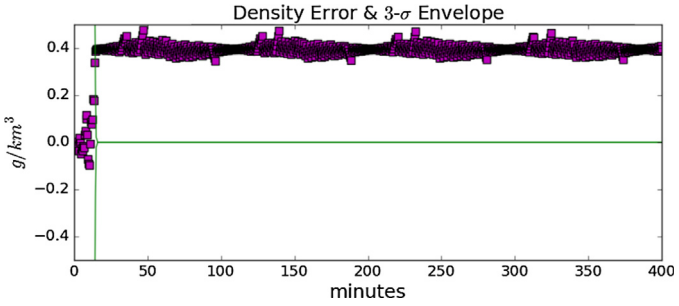

Fig. 5. PF density error and 3-σ envelope.

of particles still reveal a relatively large error that occurs cyclicly. The cyclic behavior of the error shown in Fig. 8. b (the zoomed in version of Fig. 8.a) occurs when the true density has the smallest magnitude (Fig. 2). This occurs on

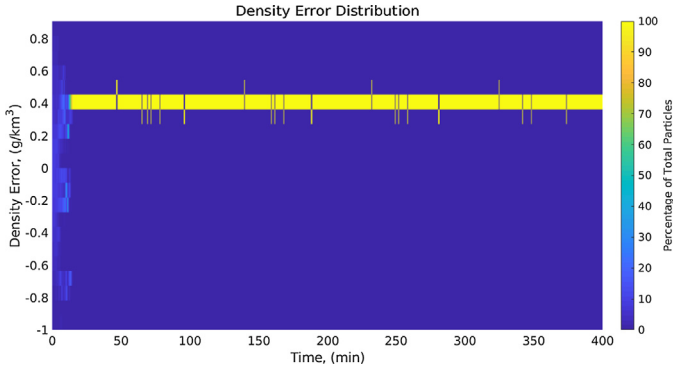

Fig. 6. PF particle evolution.

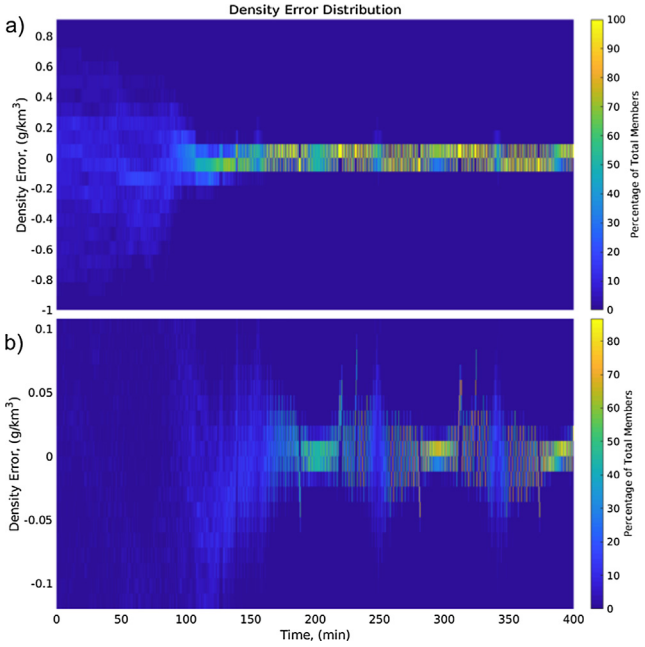

Fig. 8. POEnKF particle evolution zoomed.

the night-side near 0 degrees LST. The filter performance is degraded in regions of low density because a small density has relatively little effect on the object orbit and is therefore less observable.

A direct comparison between the performance of the PF and POEnKF is provided in Fig. 9, which shows their

Please cite this article as: S. Mutschler, P. Axelrad and T. Matsuo, A Partially Orthogonal EnKF approach to atmospheric density estimation using orbital debris, Advances in Space Research, https://doi.org/10.1016/j.asr.2020.01.021

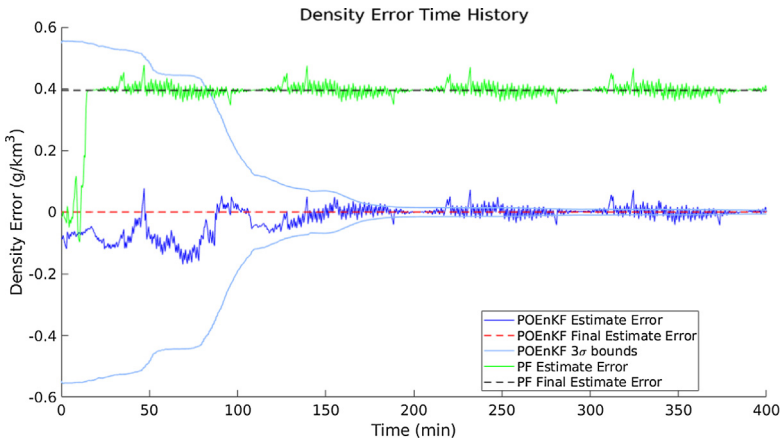

Fig. 9. PF and POEnKF performance comparison.

density estimation errors as a function of time. The black and red dotted lines represent the final errors of the PF and POEnKF, respectively. As seen in the earlier figures, the PF estimate diverges about 15 min into the run with the collapse of its covariance, and thereafter ignores the measurements and never recovers. The POEnKF performs properly, accumulating information from the measurements throughout the run, and settling near the truth with errors that are well described by the 3-sigma bounds.

This simplified version of the extended state density estimation problem illustrates the advantage of utilizing the POEnKF over the PF for high dimensional systems.

4. Full density estimation system

This section presents a more complete version of the density estimation approach. The scenario includes multiple debris objects orbiting at a fixed LEO altitude with various inclinations, right ascension of ascending nodes, etc., and therefore, expands the problem space from a single equatorial orbital path to a spherical shell encompassing Earth. Similar to the simplified example, the debris objects are propagated using two-body Keplerian dynamics with the addition of acceleration due to atmospheric drag (Eq. (31)). The partial sinusoid as the underlying atmospheric density model is replaced by the MSIS Atmospheric Model (Picone et al., 2002).

4.1. System details

The estimated states in this scenario are: the position and velocity of multiple orbital debris objects and a 2D grid of atmospheric density. We model the spherical shell of neutral density at 400 km altitude with a spatial grid parameterized by LST and latitude. An altitude of 400 km is used here, similar to Emmert et al. (2008), Morozov et al. (2013), and Pilinski et al. (2016). These parameters define a spatial grid in the sun-fixed coordinate frame. Both LST and latitude have a spatial resolution of five degrees. The resulting vector of densities, one at each grid point, contains 2701 elements, yielding a total of $2701 + 6D$ estimated elements when combined with the orbit states of each object. The grid of density elements is defined with respect to the sun in order to account for one of the major contributors of density variability, the diurnal cycle. Due to this design, the density state is modeled as stationary, requiring no forecast step for the density portion of the state, i.e. the density state portion of $\mathcal{M}$ in Eq. (11) is identity.

The debris objects simulated for this project are inspired by the objects used in the HASDM effort. Orbital characteristics (inclination, right ascension of ascending node, etc.) of 16 HASDM objects (Bowman and Storz, 2002, 2003) are simulated; however, their eccentricity is set to zero and altitude is 400 km in order to fall within the defined problem space. For example, Vanguard 2 (satellite number 00011) has a 32.8 deg inclination, 45.2 deg right ascension of ascending node, 167.0 deg argument of perigee, and is set to have a 400 km altitude and zero eccentricity. Each object is simulated with an area to mass ratio (AMR) of 0.0955 m^2/kg. Nominally, the filter also assumes this AMR value for the mass of each object (assumes the true AMR); however, an evaluation of the effect of errors in the assumed AMR is described in Section 5.6.

Azimuth (az), elevation (el), and range (R) measurements of debris objects are generated from three ground stations. The HASDM effort is able to execute a dedicated sensor tasking campaign in which 500 measurements per object per day are collected. This equates to a measurement of each object every three minutes. Therefore, we choose a three minute measurement cadence for these simulations.

4.2. Scenario use-cases

Six scenarios are explored in Sections 5.1–5.7. A brief description and the resulting root mean squared (RMS) density error is provided for each case in Table 1.

The ground track of the orbital debris in the single object scenario is shown in Fig. 10. Red stars signify three ground stations for which measurements are generated.

Please cite this article as: S. Mutschler, P. Axelrad and T. Matsuo, A Partially Orthogonal EnKF approach to atmospheric density estimation using orbital debris, Advances in Space Research, https://doi.org/10.1016/j.asr.2020.01.021

Table 1
Case study comparison.

Case	RMS Density Error (g/km^3)
Single Object	1.2
– one object	
– sensor error: 0.15 arc-seconds for az & el, 0.1 m for range	
– measurement cadence: 3 min	
– AMR: 0.0955 m^2/kg	
Multi-Object Baseline	0.14
– 16 objects	
– all objects AMR: 0.0955 m^2/kg	
Larger Sensor Error	0.42
– sensor error: 1 arc-second for az & el, 0.5 m for range	
Reduced Measurement Cadence	0.28
– measurement cadence: 6 min	
Unknown Ballistic Coefficient	0.21
– each object AMR randomly generated with particular mean & variance	
Geomagnetic Storm	3.47
– extreme geomagnetic storm	

The stations located in Canberra, Madrid, and Diego Garcia are referred to as station 1, station 2, and station 3, respectively. The ground-tracks of the 16-object scenario are shown in Fig. 11. The object trajectory is simulated for roughly one orbital period. This scenario is used for the majority of our analysis (Sections 5.3–5.7).

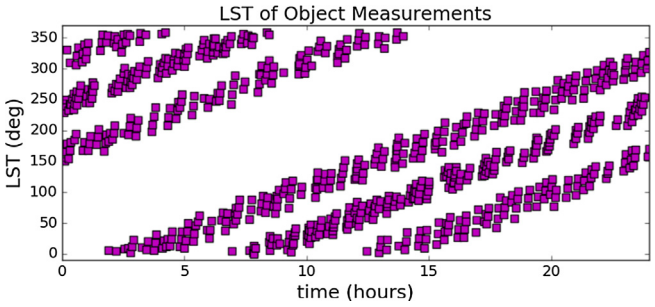

Fig. 12. Local sidereal time of all object measurements during 24 h multi-object scenario.

Fig. 12 shows the LST of each object at the times when a measurement is collected of that object. It is apparent that there is a gap in the LST of the measurements, which shifts throughout the 24 h simulation. This measurement gap is caused by the absence of sensor stations on the western side of the globe (Fig. 11). As the local time for each ground station progresses throughout the day, so does the LST of the measurements collected by each ground station. This affects the estimation error for density state elements located at local sidereal times for which there are gaps. For example, during the first 250 min of the simulation

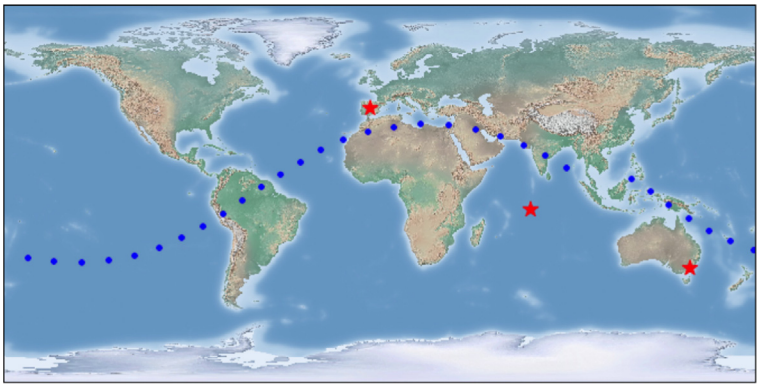

Fig. 10. Groundtrack of 90 min trajectory for single debris object scenario.

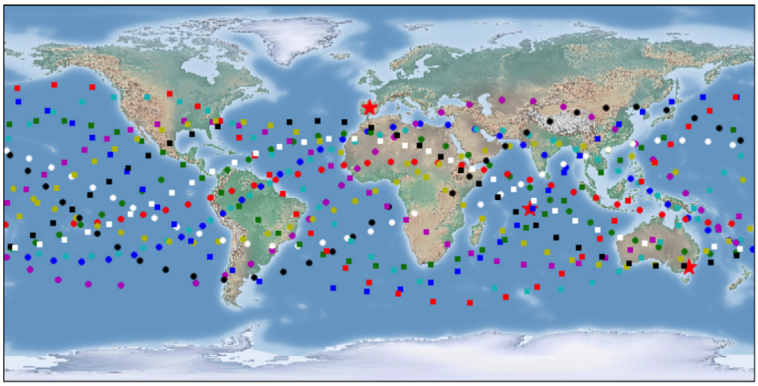

Fig. 11. Groundtrack of 90 min trajectory for 16 HASDM inspired objects.

Please cite this article as: S. Mutschler, P. Axelrad and T. Matsuo, A Partially Orthogonal EnKF approach to atmospheric density estimation using orbital debris, Advances in Space Research, https://doi.org/10.1016/j.asr.2020.01.021

there are no measurements taken of objects located between 0 and 150 deg LST. The effect of the measurement gap in LST is discussed further in Section 5.3.

4.3. System initialization

As in the simple model, a perturbation is applied to the true initial OD state so that the *a priori* state in the filter is not equal to the true initial state,

$$\vec{X}'_{OD\ 0} = \vec{X}_{OD\ 0} + p_{OD} \tag{44}$$

where the perturbation has a nonzero mean that is drawn from a normal distribution:

$$p_{OD} \sim \mathcal{N}\left(\mu_{pert\ OD}, P_{pert\ OD}\right) \tag{45}$$

$$\mu_{pert\ OD} = [100m, 100m, 100m, 0.1m/s, 0.1m/s, 0.1m/s]^T \tag{46}$$

$$P_{pert\ OD} = diag\Big(\Big[(1m)^2, (1m)^2, (1m)^2, (0.01m/s)^2, (0.01m/s)^2, (0.01m/s)^2\Big]\Big) \tag{47}$$

The MSIS model generates a density value when provided with various input parameters. These parameters include latitude, LST, altitude, day of year (DOY), F10.7 index, and the Ap index (Table 2). Latitude and LST are inherently defined for each value of the density state in the parameterization scheme.

June 24th is the date chosen for the simulation (DOY = 175). The true density field can be generated with the nominal inputs provided in Table 3. An equatorial slice of the true underlying density field generated using these nominal input parameters is shown in Fig. 13.

Similar to the OD state, a perturbation is applied to the true initial density state to produce the filter's *a priori* estimate:

$$\vec{X}'_{\rho\ 0} = \vec{X}_{\rho\ 0} + p_{\rho} \tag{48}$$

$$p_{\rho} \sim \mathcal{N}\left(\mu_{pert\ \rho}, P_{pert\ \rho}\right) \tag{49}$$

$$\mu_{pert\ \rho} = \Big[(0.1)^2, (0.1)^2, \ldots, (0.1)^2\Big] g/km^3 \tag{50}$$

Table 2
MSIS parameters for nominal density.

Parameter	DOY	Ap Index	F10.7 Index	Altitude
Value	175	17	127	400 km

Table 3
MSIS parameters for an extreme geomagnetic storm.

Parameters	Ap Index	F10.7 Index
Nominal Conditions	17	127
Extreme Geomagnetic Storm	400	273

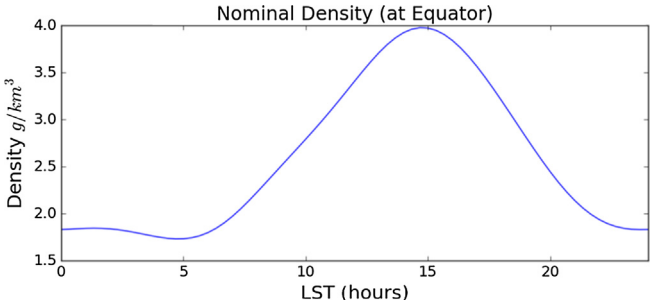

Fig. 13. Nominal density state at equator.

$$P_{pert\ \rho} = diag\Big(\Big[(0.5)^2, (0.5)^2, \ldots, (0.5)^2\Big]\Big)\left(g/km^3\right)^2 \tag{51}$$

4.4. Ensemble generation

The number of ensemble members, N, was selected via a Monte Carlo study of the density state error distribution as a function of N. It was determined that a 100-member ensemble is sufficient to represent the full state of 2701 + 6D elements, where D is the number of debris objects. The method for generating a randomly distributed ensemble is different for the two portions of our estimated state.

To generate the initial ensemble ($\chi^{(i)}_{OD\ 0}$) for the position and velocity portion of the state, 100 samples are drawn from a distribution with $\vec{X}'_{0,OD}$ mean and P_0 variance using Eq. (10). The standard deviations in P_0 correspond to the perturbations applied to the initial ensemble ($\mu_{pert\ OD}$),

$$P_0 = diag\Big(\Big[(100m)^2, (100m)^2, (100m)^2, (.1m/s)^2, (.1m/s)^2, (.1m/s)^2\Big]\Big) \tag{52}$$

The density ensemble is generated with a different approach because an appropriate covariance of the density random variable is unknown. In this case, MSIS is used to generate density values that represent the probable distribution statistics. To do so, we begin by defining an array of values for the latter four variables (DOY, F10.7 index, Ap index, and altitude).

$$\begin{aligned}
\text{DOY} &= [169, 171, 173, 175, 177, 179, 181] \\
\text{F10.7} &= [67, 83, 102, 124, 148, 172, 196] \\
\text{Ap index} &= [0, 4, 7, 14, 27, 48] \\
\text{altitude} &= [395, 396, 397, 398, 399]
\end{aligned}$$

Each parameter array is randomly sampled 100 times to generate 100 combinations of input to MSIS. Each combination produces a density ensemble member (Fig. 14). Varying these parameters produces a range of density realizations encompassing the likely true densities. A comparison between the mean of the density ensemble and the true nominal density is provided in Fig. 15.

Please cite this article as: S. Mutschler, P. Axelrad and T. Matsuo, A Partially Orthogonal EnKF approach to atmospheric density estimation using orbital debris, Advances in Space Research, https://doi.org/10.1016/j.asr.2020.01.021

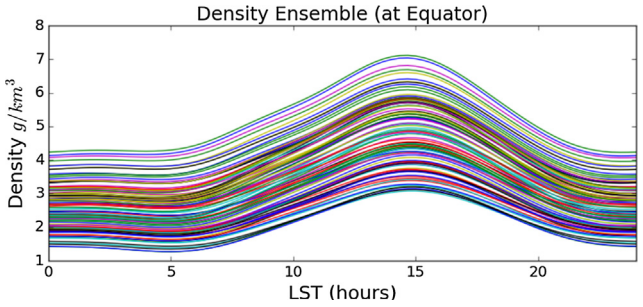

Fig. 14. Density ensemble.

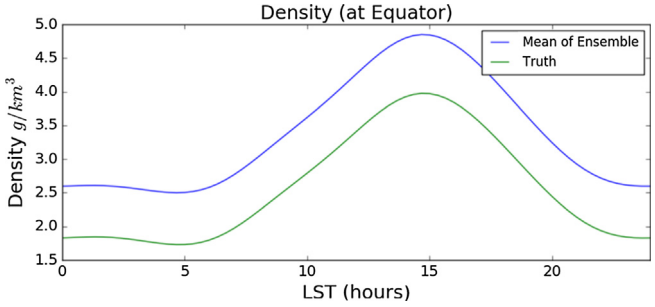

Fig. 15. Density ensemble mean and density truth.

4.5. q eigenvectors selection

The number of leading eigenvectors used for the reduced rank representation of the full ensemble in the POEnKF is determined via an analysis of the initial ensemble covariance eigenvalues. It was found that including components with eigenvalues of 1e-6 and higher is sufficient. This suggests that $q = 26$ is appropriate for the state covariance reduced rank approximation in the single object scenario and 60 leading eigenvectors for the 16 object scenario.

Proper selection of q is important because selecting a relatively small q greatly reduces computation time. However, too small of a q can also cause filter divergence because the reduced rank approximation will not adequately represent the full state behavior (Heemink et al., 2000).

5. Analysis and results

This section presents a series of scenarios in which various use cases for our tool are analyzed. These cases demonstrate the sensitivity of the POEnKF to various conditions such as constant verses nominal surveillance, single verses multi-object, sensor error, measurement cadence, knowledge of the objects' AMR, and a geomagnetic storm.

5.1. Constant surveillance: single object

This simulation includes a single debris object and constant surveillance in which there is a measurement every three minutes regardless of physical constraints or observability conditions. It is noted that due to the behavior of MSIS, the information from a single debris object at a particular location on the density grid inherently provides information for all density grid elements. The debris object completes three orbital periods throughout the simulation. There is a larger error in the density estimate during the first orbital period (first 90 min), but subsequently the solution converges and does not exceed 20% error nor the 3-σ bounds. Fig. 16 shows the percent error of the density estimate with each estimate's corresponding measurement station identified. Fig. 17 is the error of the density estimate with the same labels used to identify the station from which that estimate's measurement originated. This figure provides the estimate after the time update (black dot markers), as well as the estimate after the measurement update (square, triangle, and diamond markers indicating the ground station).

The overall RMS density error for this simulation is 0.32 g/km^3 out of an average 2.68 g/km^3 density. The RMS density error post-convergence (after 90 min) is 0.22 g/km^3. This post-convergence RMS density error is more indicative of the performance of the filter and will therefore be the error reported and used for comparison in the remaining scenarios (Sections 5.2–5.7). The performance of the OD portion of the state is illustrated below via the X position and X velocity error and covariance (Fig. 18). The remainder of the state, the Y and Z position and Y and Z velocity, have similar performance with small RMS errors of 2 m, 2 m, 3 cm/s, and 4 cm/s, respectively.

5.2. Nominal surveillance: single object

For this simulation the debris object measurements are generated only when the debris object is visible from a

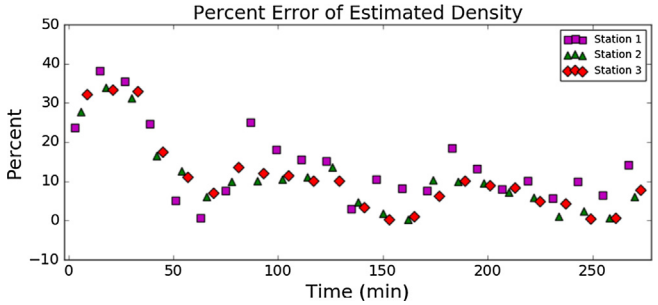

Fig. 16. Single object constant surveillance density estimate percent error.

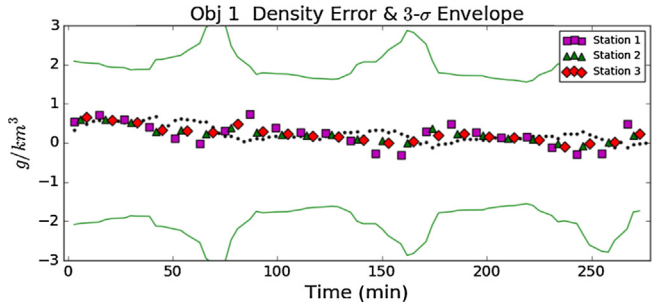

Fig. 17. Single object constant surveillance density error and 3-σ envelope.

Please cite this article as: S. Mutschler, P. Axelrad and T. Matsuo, A Partially Orthogonal EnKF approach to atmospheric density estimation using orbital debris, Advances in Space Research, https://doi.org/10.1016/j.asr.2020.01.021

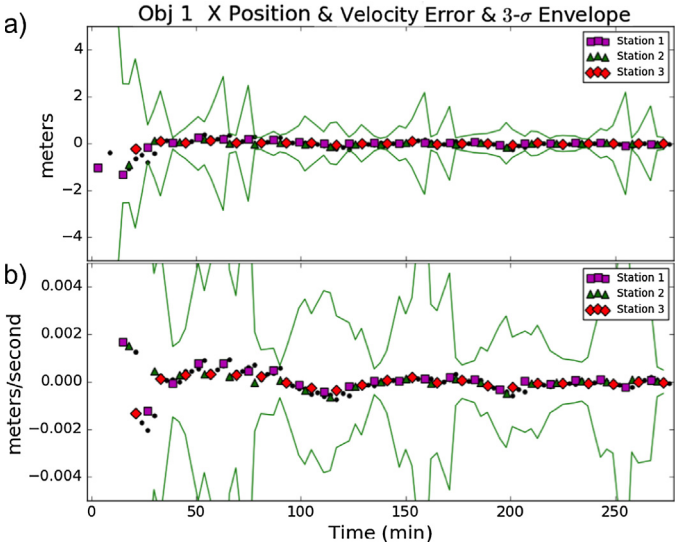

Fig. 18. Single object constant surveillance X position and velocity error and 3-σ envelope.

ground station. Therefore, the measurements do not occur every three minutes consistently throughout the simulation. This simulation is run for the same duration as the simulation in Section 5.1. As expected, the performance is worse than that with constant surveillance. The estimated RMS density error is 1.2 g/km^3 for nominal surveillance compared to 0.22 g/km^3 for constant surveillance. The estimated density error is shown in Figs. 19 and 20. Fig. 21 shows the ground track of the debris object measurements as seen by the three stations indicated by red stars.

This scenario demonstrates the need for measurements of multiple debris objects in order to estimate density to the desired level of accuracy. It is not possible to consistently task sensors to "stare" at debris objects and collect hundreds of measurements of each object every day, as is done for the HASDM effort. We aim to develop a tool capable of using sparse debris data to estimate density; our advantage being that there are thousands of debris objects to utilize for this purpose. Section 5.3 demonstrates the substantial improvement in the density estimate when data from 16 debris objects are utilized.

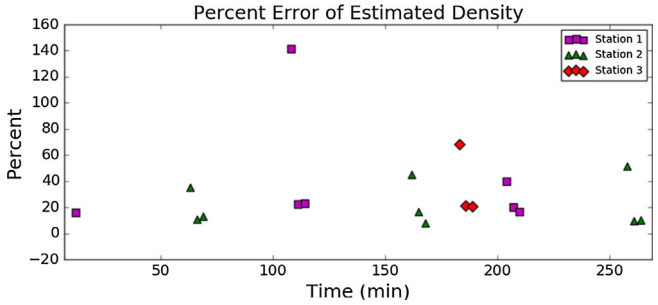

Fig. 19. Single object nominal surveillance density estimate percent error.

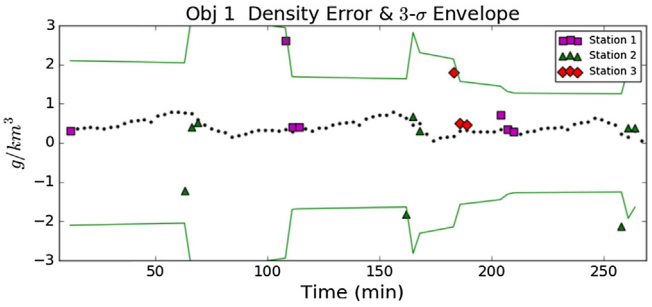

Fig. 20. Single object nominal surveillance density error and 3-σ envelope.

5.3. Nominal surveillance: multiple objects

This scenario is similar to that of Section 5.2, but with 16 HASDM-inspired objects instead of one. These objects vary in inclination, right ascension of ascending node (RAAN), and argument of perigee. This scenario is referred to as the baseline case. The overall RMS error of the density estimate is greatly reduced when using 16 debris objects compared to one object (Table 1).

Fig. 22 shows that the density estimate percent error is relatively large in the beginning of the simulation, but the filter is able to converge to a relatively low error for the remainder of the simulation. Fig. 23 shows the updated density error for the element closest to the measurement (square, diamond, and triangle symbols) and the density error of the density elements located along the Object 1 orbital path (black dots).

Fig. 24 shows the percent error of the density estimate as a function of LST. It was shown in Section 3.2 via the Simplified Problem that the filter has the smallest percent error in the density estimate when going through higher density regions, because the effect of density on the object trajectories is more observable in higher density regions. Therefore, it was expected that the filter would have the lowest percent error at local sidereal times near noon (highest density) for this multi-object scenario. However, we find that the lowest percent error in the density estimate actually occurs when measurements are taken of debris objects in *low density regions* (near zero deg LST). This is contradictory to what is expected, but is explained by the gap in measurements between 40 and 150 deg LST. The measurements taken directly after the gap have a high percent error when the lowest percent error is what is expected. If there were consistent measurements throughout all LST values, then the lowest percent error in the density estimate would occur around noon (180 deg LST) as seen in the Simplified Example. The cause of this measurement gap in LST was described in Section 4.2. The ground track of the measurements for each of the sixteen objects is shown in Fig. 25.

The RMS density error over the entire grid, for each measurement time is shown in Fig. 26. This plot is indicative of the overall performance of the filter because it captures the filter's performance over the entire density state-space. Previous figures focused on the RMS error

Please cite this article as: S. Mutschler, P. Axelrad and T. Matsuo, A Partially Orthogonal EnKF approach to atmospheric density estimation using orbital debris, Advances in Space Research, https://doi.org/10.1016/j.asr.2020.01.021

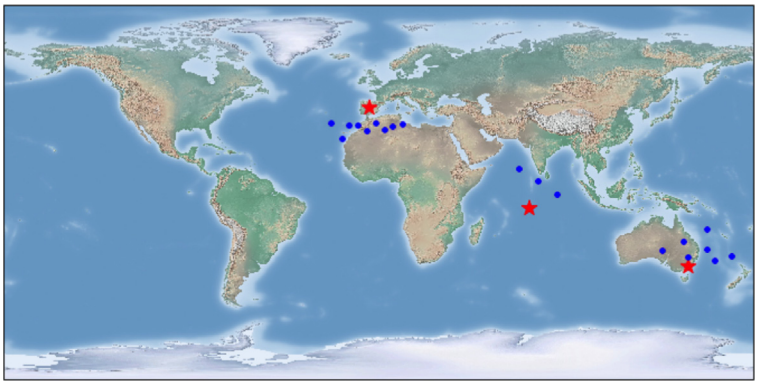

Fig. 21. Single object nominal surveillance ground track of debris object measurements.

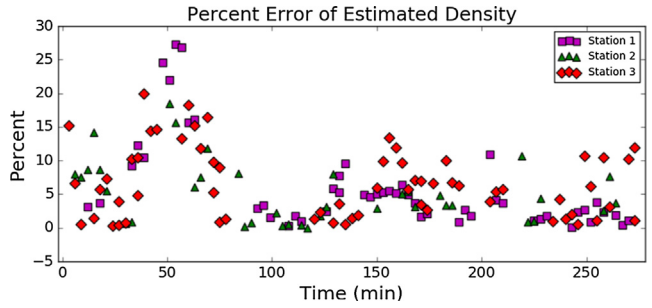

Fig. 22. Multi-object nominal surveillance density estimate percent error.

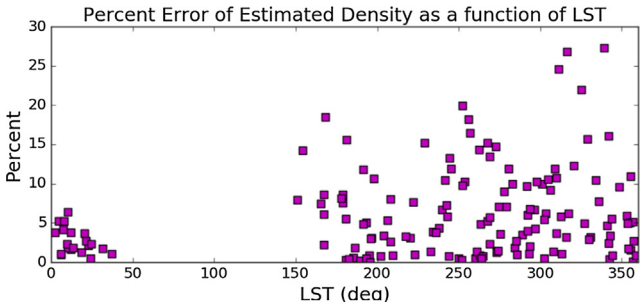

Fig. 24. Density percent error as a function of LST.

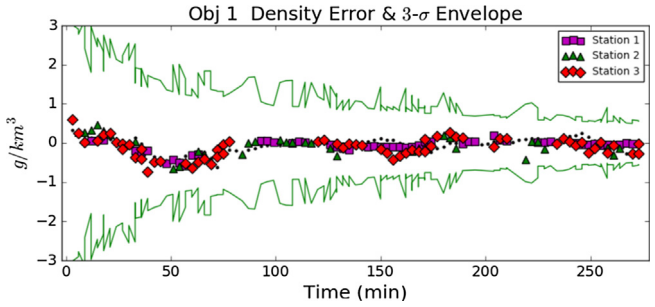

Fig. 23. Multi-object nominal surveillance density error and 3-σ envelope.

for a particular density element, or location on the spatial grid, as a function of time. It is apparent that the full density state error follows the same trend shown in Fig. 22, converging after 90 min, or one orbital period.

5.4. Sensor error study

This scenario introduces a larger sensor error into the baseline multi-object scenario, demonstrating the sensitivity of the density estimate to measurement error and noise. The azimuth and elevation sensor error standard deviation is increased from 0.15 arc-seconds to 1 arc-second. Likewise, the range sensor error is increased from a standard deviation of 0.1 meters to 0.5 meters.

It is expected that the density estimate error increases with the same magnitude of the sensor error. Because density has a relatively small contribution to the debris object dynamics, any additional sensor error will impact the accuracy of the density estimate. This is shown in Fig. 27. The error in the density has increased throughout the simulation compared to the baseline case.

5.5. Measurement cadence study

To study the effect of measurement cadence, we increased the time between measurements from three minutes to six minutes. Even though there are measurements from sixteen objects, the measurements are more sporadic (Fig. 28). The overall RMS density error increases from 0.14 g/km^3 for the baseline multi-object scenario to 0.28 g/km^3.

5.6. Unknown ballistic coefficient

In each of the prior scenarios, the filter assumes it knows the true AMR of each object (0.0955 m^2/kg). This scenario simulates objects of different AMRs while the filter still assumes an AMR of 0.0955 m^2/kg for each debris object. Each AMR is drawn from a normal distribution with 0.0955 m^2/kg mean (mean AMR error of zero) and 0.015 m^2/kg standard deviation. The standard deviation is equal to roughly 15% of the total AMR. Fig. 29 shows that the filter has the highest error within the first 40 min and then is able to resolve the density estimate to within 15–20% error. The magnitude of error is about 5% higher than

Please cite this article as: S. Mutschler, P. Axelrad and T. Matsuo, A Partially Orthogonal EnKF approach to atmospheric density estimation using orbital debris, Advances in Space Research, https://doi.org/10.1016/j.asr.2020.01.021

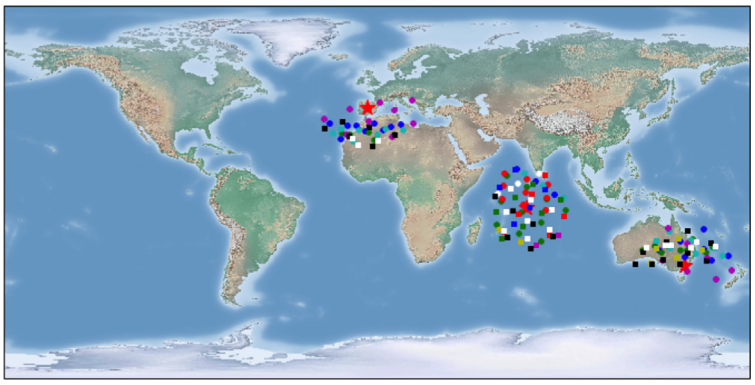

Fig. 25. Multi-object nominal surveillance ground track of debris objects measurements.

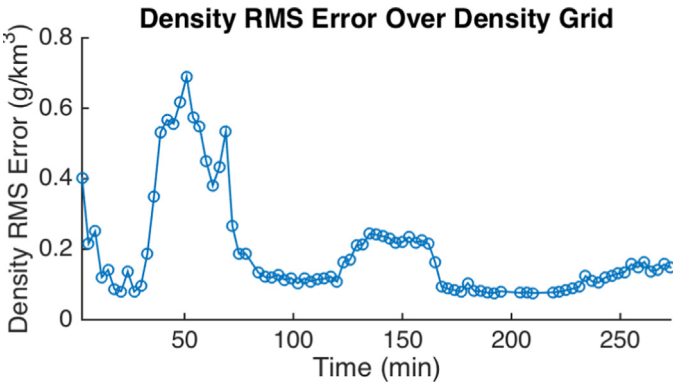

Fig. 26. The RMS density error over the entire spatial grid as a function of time for the Baseline Case.

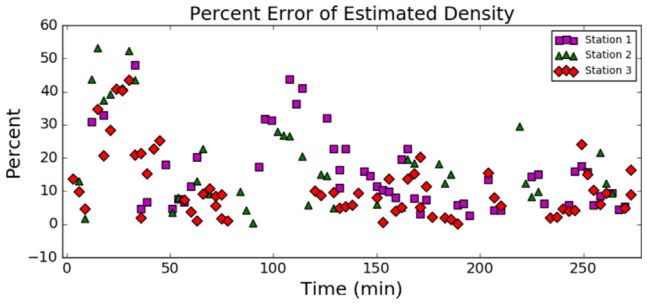

Fig. 27. Sensor error study density estimate percent error.

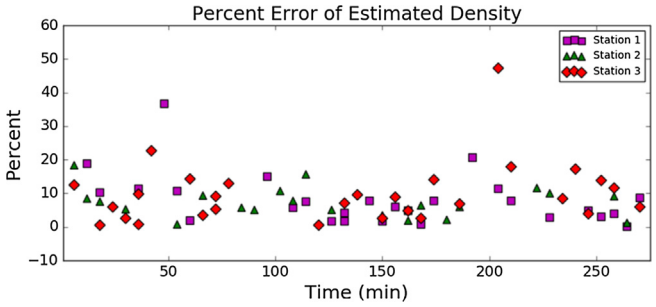

Fig. 28. Measurement cadence study density estimate percent error.

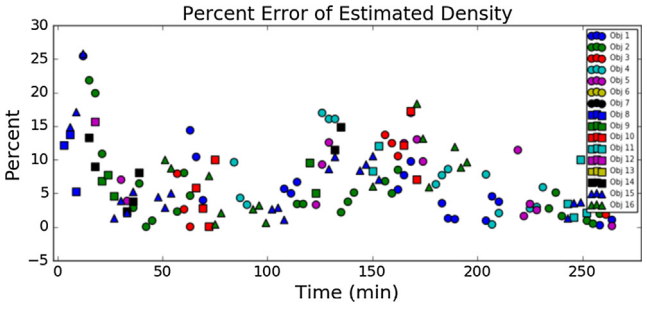

Fig. 29. Unknown ballistic coefficient study density estimate percent error.

the baseline multi-object scenario throughout the simulation (Table 1 and Fig. 30).

This scenario shows that the filter should still be able to estimate the density to a reasonable level of accuracy for a real-world case where the debris object ballistic coefficients are not known precisely. A best guess of the ballistic coefficients would be used in the filter. These ballistic coefficients are from the bootstrap process described in Section 2.

5.7. Geomagnetic storm

This scenario simulates an extreme geomagnetic storm that ramps up to Ap and F10.7 indices of 400 and 273, respectively (NOAA Space Weather Scales; Thompson; Space Weather Indices).

The geomagnetic storm begins building at approximately 200 min into the simulation and continues for the remainder of the simulation (Fig. 31). Once the geomagnetic storm begins, the density estimation error increases rapidly as the filter attempts to compile enough information to sense the true density. After the storm reaches a steady-state, around 500 min into the simulation, the filter takes about one orbital period, 90 min, to correct the density estimates (Fig. 32). From this point forward, the density estimate stays within 30%-40% error and to within 20% error by the end of the simulation (2225 min). The RMS density error over the full density state for each measurement time is shown in Fig. 33.

Please cite this article as: S. Mutschler, P. Axelrad and T. Matsuo, A Partially Orthogonal EnKF approach to atmospheric density estimation using orbital debris, Advances in Space Research, https://doi.org/10.1016/j.asr.2020.01.021

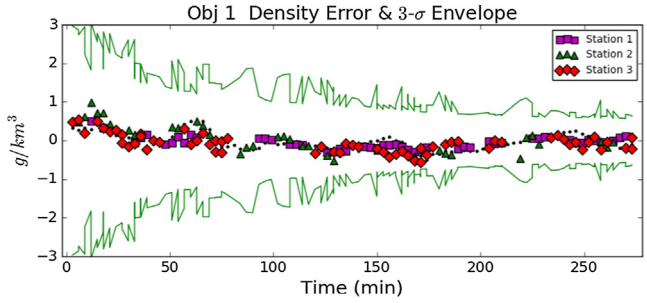

Fig. 30. Unknown ballistic coefficient study density error and 3-σ envelope.

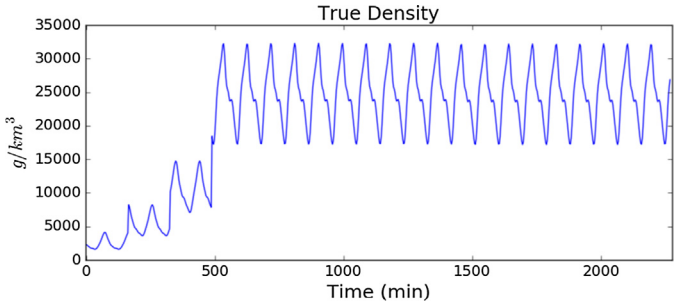

Fig. 31. True density during extreme geomagnetic storm.

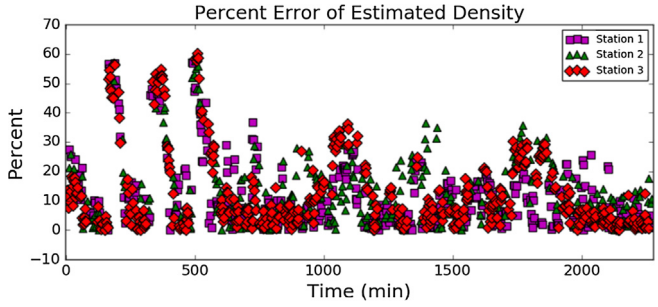

Fig. 32. Geomagnetic storm density estimate percent error.

5.8. Results summary

Table 1 summarizes the results for case studies exploring the filter's dependence on sensor error, measurement cadence, ballistic coefficient information, and a geomagnetic storm. It is found that increasing the sensor error by an order of magnitude also increases the RMS density error by roughly half an order of magnitude. When the measurement cadence is reduced by 50%, the RMS density error doubles. The density error increases by 50% when the ballistic coefficient is known within 15% of its true value. By far, the filter had the most difficulty in the geomagnetic storm case, but this is to be expected when the density is increasing by an order of magnitude within just a couple hours. Fig. 34 shows the RMS error over the entire spatial grid of density elements as a function of time for comparable cases (Sections 5.3–5.6).

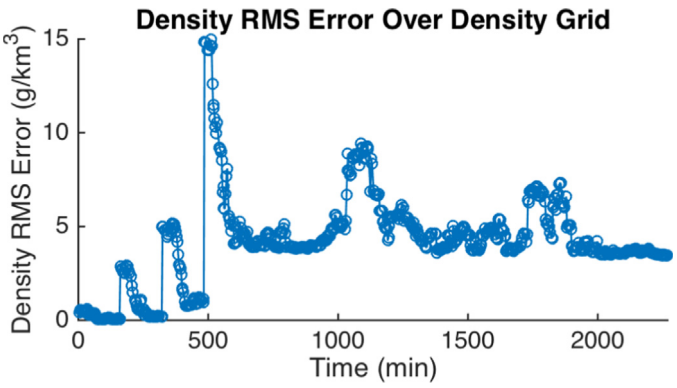

Fig. 33. The RMS density error over the entire spatial grid as a function of time for the Geomagnetic Storm Case.

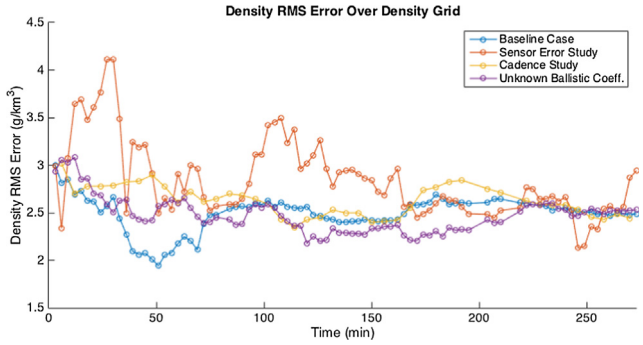

Fig. 34. The RMS density error over the entire spatial grid as a function of time for various case studies.

6. Conclusion

The POEnKF proves to be a suitable method for estimating a large state comprised of debris object states (position and velocity) and a grid of atmospheric density. This particular filter avoids a nonpositive definite matrix while still maintaining enough information, or covariance eigenvectors, to allow for the regions of different density throughout the grid to be effectively estimated. Not only is the POEnKF able to estimate disparate regions of density, but it is also capable of tracking rapid changes in global density due to an extreme geomagnetic storm.

Overall, the filter use cases demonstrate the tool's effectiveness in determining what criteria (sensor error, measurement cadence, ballistic coefficient knowledge) are required to achieve a certain level of accuracy in the density estimate. In Section 5.4, it is shown that if a larger measurement error, is applied the density estimate error increases. Likewise, if the ballistic coefficient is not known precisely, the error grows proportionally. This is due to the direct correlation between atmospheric drag and both the ballistic coefficient and atmospheric density. These parameters are coupled (Eq. (1)).

In conclusion, it has been shown that using debris objects tracking data can greatly improve our real-time

Please cite this article as: S. Mutschler, P. Axelrad and T. Matsuo, A Partially Orthogonal EnKF approach to atmospheric density estimation using orbital debris, Advances in Space Research, https://doi.org/10.1016/j.asr.2020.01.021

estimate of atmospheric density compared to assuming a particular density model which will likely be incorrect when the atmosphere is disturbed. The dispersion of multiple debris objects provides global information about the atmospheric density at any given time, instead of at a single debris object location. If a geomagnetic storm occurs, this tool can provide more accurate density estimates than that of a simple exponential atmospheric density model or MSIS (when calm conditions are assumed). The work presented here explores the POEnKF performance when using information from only 16 debris objects, the research vision is to utilize information from all debris objects. Although observations of particular debris objects are sporadic, observations of the overall debris population are collected regularly. Our tool can utilize this influx of debris object information to provide improved density estimates consistently. Enhanced knowledge of near real-time atmospheric density behavior will allow for improved predictions of all objects, not just orbital debris.

The next phase of planned research is to incorporate a physics-based atmospheric model in the forecast step. This version of the tool will involve estimating accelerations from debris object measurements and using these accelerations to infer forcing parameters, such as Kp and F10.7 indices, of the physics-based model, TIE-GCM. Similar to the current tool, the product of our new tool will be an improved time-series estimate of atmospheric density, with the addition of a physics driven forecasting ability.

References

Bowman, B., Storz, M.F., 2002. Time Series Analysis of HASDM Thermospheric Temperature and Density Corrections. In: AIAA/AAS Astrodynamics Specialist Conference.

Bowman, B., Storz, M.F., 2003. High accuracy satellite drag model (HASDM) review. Adv. Astronaut. Sci. 116, 1943–1952.

Emmert, J., Picone, J., Meier, R., 2008. Thermospheric global average density trends, 1967–2007, derived from orbits of 5000 near-Earth objects. Geophys. Res. Lett. 35, L05101.

Evensen, G., 1994. Sequential data assimilation with a nonlinear quasi-geostrophic model using monte carlo methods to forecast error statistics. J. Geophys. Res. 99 (10), 143–162.

Evensen, G., 2009. Data Assimilation – The Ensemble Kalman Filter. Springer.

Gordon, N., Salmond, D., Smith, A., 1993. A novel approach to nonlinear/non-Gaussian Bayesian state estimation. lEE Proc. Radar Signal Process. 140 (2), 107–113.

Gaspari, G., Cohn, S.E., 1999. Construction of correlation functions in two and three dimensions. Quart. J. Roy. Meteorol. Soc. 125, 723–757.

Houtekamer, P., Mitchell, H.L., 2005. Ensemble Kalman Filtering. Quart. J. Roy. Meteorol. Soc. 131, 3269–3289.

Houtekamer, P., Zhang, F., 2016. Review of the Ensemble Kalman Filter for Atmospheric Data Assimilation. Month. Weather Rev. 144, 4489–4532.

Heemink, A., Verlaan, M., Segers, A., 2000. Variance Reduced Ensemble Kalman Filtering. Month. Weather Rev. 129, 1718–1728.

Linares, R., Jah, M., Crassidis, J., Leve, F.A., Kelecy, T., 2014. Astrometric and photometric data fusion for inactive space object feature estimation. Acta Astronautica 99, 1–15.

Matsuo, T., 2014. Upper atmosphere data assimilation with an ensemble Kalman filter. In: Qian, L., Burns, A.G., Emery, B.A., Foster, B., Lu, G., Maute, A., Richmond, A., Roble, R.G., Solomon, S., Wang, W., 2014. Modeling the Ionosphere-Thermosphere System. doi:https://doi.org/10.1002/9781118704417.ch7.

Mehta, P., Linares, R., 2017. A methodology for reduced order modeling and calibration of the upper atmosphere. Space Weather 15 (10), 1270–1287.

Morozov, A., Ridley, A., Bernstein, D., Collins, N., Hoar, T., Anderson, J., 2013. Data assimilation and driver estimation for the Global Ionosphere-Thermosphere Model using the Ensemble Adjustment Kalman Filter. J. Atmos. Sol.-Terres. Phys. 104, 126–136.

NOAA Space Weather Scales, 2011. Space Weather Prediction Center www.swpc.noaa.gov/noaa-scales-explanation (accessed 10.1.18).

Picone, J.M., Hedin, A.E., Drob, D.P., Aikin, A.C., 2002. NRLMSISE-00 empirical model of the atmosphere: statistical comparisons and scientific issues. J. Geophys. Res. 107 (A12), 1468.

Pilinski, M., Crowley, G., Sutton, E., Codrescu, M., 2016. Physics-based assimilative atmospheric modeling for satellite drag specification and forecasts. Adv. Astronaut. Sci. 156, 4405–4423.

Storz, M.F., Bowman, B.R., Branson, J.I., Casali, S.J., Tobiska, W.K., 2005. High Accuracy Satellite Drag Model (HASDM). Adv. Space Res. 36 (12), 2497–2505.

Sutton, E., 2018. A new method of physics-based data assimilation for the quiet and disturbed thermosphere. Space Weather 16 (6), 736–753.

Thompson, R., Space Weather Indices, Australian Government Bureau of Meteorology www.sws.bom.gov.au/Educational/1/2/4 (accessed 10.1.18).

Vallado, D.A., 2013. Fundamentals of Astrodynamics and Applications. Space Technology Library.

Volkov, I., 2004. Earth Upper Atmosphere Density Model for Ballistic Support of Flights of Artificial Earth Satellites (GOST R 25645.166.2004). Publishing House of the Standards., Moscow.

Yurasov, V., Nazarenko, A., Cefola, P., Alfriend, K., 2005. Density Corrections for the NRLMSIS-00 Atmosphere Model. In: AIAA/AAS Space Flight Mechanics Conference. AAS 05-168.

Yurasov, V., Nazarenko, A., Alfriend, K., Cefola, P., 2006. Direct Density Correction Method: Review of Results. In: 57th International Astronautical Congress Conference.

Please cite this article as: S. Mutschler, P. Axelrad and T. Matsuo, A Partially Orthogonal EnKF approach to atmospheric density estimation using orbital debris, Advances in Space Research, https://doi.org/10.1016/j.asr.2020.01.021